

A Smart Wing Rib Structure Suitable for Design for Additive Manufacturing (DfAM) Process

Ramona Dogea^{1*}, Xiu T Yan^{1*} and Richard Millar²

¹University of Strathclyde, Department of Design, Manufacture and Engineering Management (DMEM), Glasgow, Scotland

²National Manufacturing Institute Scotland – University of Strathclyde

ABSTRACT

Additive manufacturing has been adopted widely across various industries for producing parts mainly due to their ability to create complex geometries, eliminate material wastage and enable faster production rate, among others. Additive manufacturing has also increased design solution space by enabling exploration of mechatronic solutions for mechanical structures. This includes the integration of smart devices into wing structures to achieve a data-driven predictive maintenance-based system. For this, there is still the need to continuously explore various ways of integrating sensory capability into a mechanical structure during the manufacturing processes to ensure improvement and reliability of aircraft components. The scope of this paper was to analyse different wing rib geometries and the influence of embedding sensory capability via design for additive manufacturing process. In this work, three wing rib geometries with cut-outs and for sensory placement were designed and analysed to estimate their equivalent stress and deformation when such sensory locations are introduced. The results confirm the idea that it is feasible to introduce holding cavities for structural performance monitoring sensors without compromising the structural design requirements. The results also show that deformation and stress are highly dependent on the rib thickness and the insertion of sensory locations.

*Corresponding authors

Ramona Dogea, Xiu T. Yan, University of Strathclyde, Department of Design, Manufacture and Engineering Management (DMEM), Glasgow, Scotland. E-mail: ramona.dogea@strath.ac.uk; x.yan@strath.ac.uk

Received: December 06, 2021; **Accepted:** December 11, 2021; **Published:** December 20, 2021

Keywords: Wing rib, additive manufacturing, embedded sensors, Industry 4.0

Introduction

Manufacturing companies of commercial aircrafts are governed majorly by regulations and design standards associated with the design process, maintenance and operational challenges [1]. Aerospace conventional preventive maintenance normally takes up to 5000 flight hours/part replacement which usually relies on history and statistics and does not take into consideration the day-to-day operating conditions of parts [2]. With the advancement in technology, the aerospace industry is now adopting a more proactive approach towards aircraft manufacturing by slowly drifting away from the condition-based preventive maintenance system to a data-driven predictive maintenance-based system. This modern predictive maintenance systems are aided by technological platforms like digital twins which relies on sensory information [3]. There is therefore the need to continuously explore various ways of integrating sensory capability into manufacturing design processes to improve reliability of aircraft components. Embedding sensors within a desired location leads to the ability of an end user to monitor specific critical regions such as high temperature and pressure.

Additive manufacturing (AM) is being actively explored to be used in aerospace when fabricating structural components to

create possibilities for adding value to the product compared to traditional manufacturing processes. AM enables a more integrated lightweight design and it reduces the number of components in a system [4].

The aircraft wing structure consists of spars, ribs, stringers and the skin. Wing structures are subject to different types of loads, such as aerodynamic loads, fuel loads, engine loads, landing gear loads and inertial loads of both structural and non-structural masses [5]. Within the wing box components, the rib provides support to the skin structure and transfer the loads from the skin to the spars. Aluminium alloys are widely used to manufacture the aircraft wing ribs [6]. Wing ribs are vital fundamental components of every aircraft wing which are tasked to perform specific functions whilst also ultimately withstanding mechanical loading in service. The integrity of the wing rib components thus becomes an important consideration during design and manufacturing processes to ensure adequate provision for compensations in terms of material selection, deformation and loading under various forces. Numerical techniques like finite element model (FEM) offers a sophisticated approach to characterising the stress and deformation values of wing ribs subjected to complex loading conditions [7].

ANSYS engineering software suite based on FEM was used in this work to analyse wing rib loading conditions. The adoption of numerical methods like FEM provides more accurate approximate

solutions for different forms of elasticity problems. FEM entails the aggregation of finite elements, estimation of partial differential equations (PDEs) via simultaneous algebraic equations in order to numerically evaluate elasticity problems [8]. The main advantage of using numerical approaches such as FEM includes the capability of finding solutions to arbitrarily complicated problems for which analytical solutions are not readily suitable, time and cost savings [9].

This paper explores new design solutions for wing ribs, considering possibly deploying additive manufacturing for ribs focusing on the stress and deformation requirements. The rib design is based on the NACA 0018 airfoil for three different geometries: 5 mm thickness with 10 mm upper and lower caps, 4 mm thickness with 8 mm upper and lower caps and 3 mm thickness with 6 mm upper and lower caps. The purpose is to answer the following research questions: *What is the stress and deformation under operating conditions? How does the sensor location influence the stress distribution of wing ribs? How does rib thickness influence stress and deformation?*

The objective of this paper is to identify the most suitable rib geometry for embedded sensory capability into additive manufacturing process. Another research question is how the embedded sensory location adds value to wing ribs and how it leads to AM. Details are presented in the results and discussion section.

This work is structured into the following sections: introduction, literature review, materials and methods, results and discussion, conclusions and further work, and references.

Literature Review Wing Ribs Design

Research studies are nowadays focused on ribs and spars rather than other components. Ribs are a crucial component since it keeps the airfoil shape and it withstands wing torsion together with skin and spars. Besides, it transfers aerodynamic loads from the skin to the structure [10]. Rib selection and its manufacturing method depend on loads, design solution, available equipment, experience and costs. Generally, form and plate ribs are designed considering stiffening profile and low loads, whilst forged or machined ribs are used for very high loads [11]. To begin with the rib design, researchers refer to the National Advisory Committee for Aeronautics (NACA) airfoils which are standardised airfoil shapes designed for aircraft wings. Besides, in order to reduce manufacturing efforts, wing weight and costs, ribs with cut-outs are used [12,13]. In this work, the rib design with cut-outs was also used to ensure weight reduction and to incorporate sensory locations for enhanced wing capability. Structural health monitoring (SHM) technology is essential for reducing the risk of catastrophic failures and for improving the safety of structures by detecting damage before it reaches a critical state. The flight environment is very harsh due to large changes in humidity, temperature, pressure, speed, and loading conditions. These effects cause a lot of stress to the aircraft frame. For companies, this will translate to cost saving on maintenance and improvement in safety of their operations [14]. This will serve as value creation on their products and services, as well as saving costs on unplanned maintenance which may result in longer operations downtime.

For the fabrication of customised parts with intricate geometrical features and graded material composition, the adoption of additive manufacturing (AM) technologies is usually ideal. Depending

on the material and structure, novel designs for manufacturing processes could be introduced to ease the fabricability of components in order to increase the benefits of AM capabilities. The major purpose of the design for additive manufacturing (DfAM) should be to “maximise product performance through the synthesis of shapes, sizes, hierarchical structures, and material compositions, subject to the capabilities of AM technologies” [15]. Hence, the intentions of DfAM are realised by identifying the distinct AM capabilities and correlating them to the design opportunities and their effects. A previous work has classified DFAM into three segments: system design, part design and process design [16]. System design refers to which component should be manufactured using AM and what limitations are. Part design deals with finding the best design solution for a single part, while process design involves how design and other characteristics of the components for the manufacturing process are best considered. This paper considers two segments: part design and as future work process design. After reviewing the literature, the focus was to keep research linked to the area of optimisation of structural components for aircraft wing ribs and AM technologies.

In the aerospace industry, AM is used to produce metallic critical parts in engineering practice. The table below shows a summary of the current trends [17]:

Table 1. Overview of AM for metallic materials (‘X’: applicable; ‘-’: not applicable).

AM technique	Metallic material		
	Steel	Titanium	Aluminium
Selective Laser Melting (SLM)	X	X	X
Electron Beam Melting (EBM)	X	X	-
Laser Metal Deposition (LMD)	-	X	-

In the aerospace industry, to fabricate aluminium parts the most appropriate process is SLM, a layer-by-layer process, which will be involved at the process design stage. The fabrication of smart structures using AM technique can allow the flexibility of embedding sensors within a structure without compromising the structure and/or functionality, while using traditional manufacturing by placing sensors increases the possibility of disturbing the normal operation of systems due to sensors placement design [18]. Before re-designing the manufacturing process for wing ribs, it is necessary to explore the most suitable geometry by analysing its stress and deformation.

Meshing

One important aspect when performing simulations of any structural object or body is the mesh type. Meshing is the process of discretisation of a solid object geometry into smaller pieces for getting better accuracy results. The mesh is formed by a group of nodes and elements [13]. The accuracy of the finite element analysis can be improved by using a finer mesh or a higher order element. Another issue relating to meshing is the FEA solving convergence. It is the point at which results are not significantly different by an increase in the number of elements. To assess the accuracy of the mesh, the element quality index is used, which gives a value between 0 and 1. The suitability of the element is better when its quality index is closer to 1. The quality index of each element is calculated considering its volume and edge length [19].

There are already researchers who studied the mesh type and performance for wing ribs. Carneiro and Gamboa used different mesh approaches for three different rib topologies: 20-node hexahedron, 15-node prism and 10-node tetrahedron. Their results show that the mesh convergence and the quality index associated to the element type are highly dependent on the solid geometry and the number of elements. They concluded that the tetrahedral order had lower quality index (0.49) than the hexahedron (between 0.92 and 0.94) and prism (0.91 up to 0.95) orders [20]. Dharmendra et al., meshed the rib using edge sizing and face meshing method with tetrahedral elements. They consider the total deformation to locate the convergence point. The average element quality of their mesh is 0.7814 [7]. Sharma and Garg used the quad type, but they did not consider the meshing quality [13].

Rib Simulation under Loading Conditions

The scope of simulations is to determine the behaviour of the wing rib under loading conditions. For the wing rib model, there are studies that consider as boundary condition for the acting load a shear force applied to the leading edge, while the trailing edge is fixed [12]:

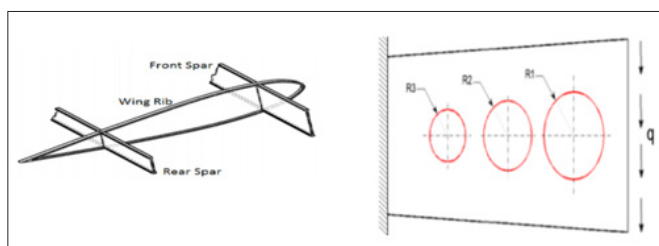


Figure 1: Boundary conditions for wing rib analysis [12].

Other studies considered a rotational velocity at the leading edge and the trailing edge as fixed support, or the leading and trailing edges of the rib are fixed, while concentrated loads are applied [21, 6]. There are researchers who simulate the entire wing. The simplest wing model for plausible simulation results is a rectangle. Moreover, it has been stated that an aircraft wing should have between five and twenty ribs so that the mass can be optimised [22]. For this work, the wing will be designed with five ribs to keep the model as simple as possible. In [23] the optimal spacing between ribs for a rectangular aircraft wing was found to be 400 mm. This value will be also used for the model in this work. For the wing, it is necessary to consider the lift and drag in order to dimension the components in the wing box. Around the airfoil, the lift has a characteristic pressure distribution that can be considered as two forces: lift and drag. The total lift force can be estimated through the aircraft weight, and each aircraft wing must withstand half of the total aircraft weight [24, 25]. To obtain an equivalent force for the boundary condition in this work, the Boeing 747-400 aircraft was considered. The applied lift force to the upper wing surface of the Boeing 747-400 is applicable to the simulation model profile NACA 0018 by considering the upper wing surface of this model. For this aircraft, the operating empty mass is $m_{Boeing} = 183,500$ kg and the upper wing surface 511 m² [26, 27].

When validating parts for DfAM through simulations under in-flight loading conditions, maximum stress and maximum deformation are usually considered. The maximum stress must be lower than the tensile ultimate strength of the material [28].

The maximum deformation of a wing is compared to the half wingspan to verify the loading conditions [29].

Embedded Sensory Capability into AM Processes for Wing Rib Design

In Stoll et al. a general process to integrate sensors during AM with Selective Laser Sintering (SLS) processes is presented [30]. It is mentioned that the integration of functional parts, like sensors or other active systems for further part optimisation, are considered as very beneficial in order to amplify the application possibilities of SLS parts:

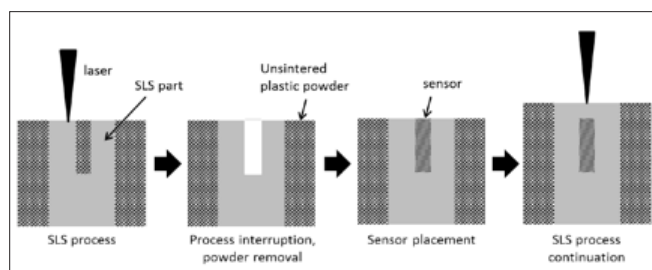


Figure 2: Process steps for integration of external parts into SLS parts [30].

Juhasz et. al. fabricated a proof-of-concept tensile bar with an embedded thick-film printed strain sensor using Directed Energy Deposition (DED) to demonstrate the potential for digital fabrication of multi-functional metal structures within a single manufacturing system without tooling [31].

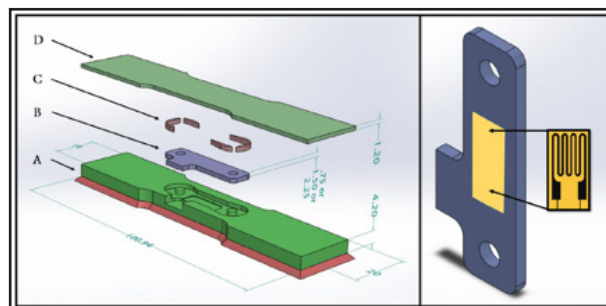


Figure 3: Schematic process for integrated sensor (left) and view of sensor plate with printed sensor and location [31].

In Cavdir, D. an accelerometer sensor is embedded during a hybrid AM process [32]. In this case, the sensor is provided with a housing in form of a pocket to protect the sensor against environmental conditions. For that, modifications in the embedded process were required, such as pausing the print at the right time and location. It is shown that the pausing process provided better results when the pause command is handled by modifying the G-code, instead of using manually the printer's control panel.



Figure 4: Embedded accelerometer manufactured using hybrid AM method [32].

Metallic components with embedded sensors or smart parts can be a beneficial tool for monitoring harsh environments in the aerospace industry. A placement of a sensor in metallic components was developed in [33] using powder bed fusion (PBF) additive manufacturing to demonstrate the applicability in harsh environments. In their work, a smart injector was fabricated to test the pressure and sensing capabilities using Electrode Beam Melting (EBM) and Selective Laser Melting (SLM).

Embedding sensor by means of both AM processes can prolong the life cycle when used in harsh/hard-to-reach environments and provide valuable performance monitoring data to improve the life cycle. Internet of Things (IoT) is known as a key enabler for the digital transformation. The collection and aggregation of large amount of data from products to the manufacturing system level allow the creation of smart models. In general, a smart asset in manufacturing can be achieved by means of four elements: (1) a sensor network installed in the physical assets to collect data, (2) an IoT device to connect the physical assets to the Internet and to transmit collected data, (3) data analysis to convert data into information and to make predictions, and (4) hardware for data visualization [34].

There are already Internet of Things (IoT) Micro-Electro-Mechanical Systems (MEMS) with tiny size that are used in aerospace applications. They are known as smart dust, and they integrate sensors, communication, control and battery [35]. Example of smart dust that is used in health monitoring systems was developed by NASA in cooperation with the University of California Berkeley. These sensors can measure a number of physical or chemical stimuli such as temperature, humidity, ambient light, vibration, acceleration, or air pressure. There are a variety of potential applications: inventory control and product monitoring, surveillance and security, internal spacecraft monitoring, and weather modelling and monitoring [36]. Although these sensors are being used in aerospace applications, its access is limited due to security, privacy and legal issues [37]. In this project similar sensory solutions will be used since the scope of the project is a small-scale demonstrator for academic purposes.

Materials and Methods

Design of a Wing Rib with Embedded Sensory Capability

The NACA 0018 profile was selected because of its symmetrical geometry with respect to the chord. Table 2 shows the surface coordinate points for this profile:

Table 2: Airfoil surface coordinates points for NACA 0018

x	y
1	0
0.95	0.0121
0.9	0.02172
0.8	0.03935
0.7	0.05496
0.6	0.06845
0.5	0.07941
0.4	0.08705
0.3	0.09003
0.25	0.08912
0.2	0.08606
0.15	0.08018

0.1	0.07024
0.075	0.063
0.05	0.05332
0.025	0.03922
0.0125	0.02841
0	0
0.0125	-0.02841
0.025	-0.03922
0.05	-0.05332
0.075	-0.063
0.1	-0.07024
0.15	-0.08018
0.2	-0.08606
0.25	-0.08912
0.3	-0.09003
0.4	-0.08705
0.5	-0.07941
0.6	-0.06845
0.7	-0.05496
0.8	-0.03935
0.9	-0.02172
0.95	-0.0121
1	0

After plotting the coordinate points in Table 2, the resultant airfoil profile for the NACA 0018 is shown in Figure 5. For the initial proposed design, a sketch with three circles and two triangular cut sections with different dimensions and spacing were employed.

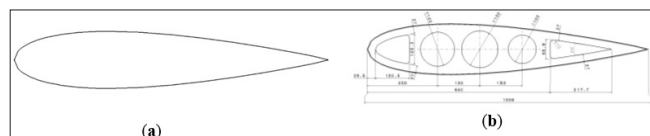


Figure 5: (a) NACA 0018 Profile; (b) Wing rib design with cut-outs (dimensions in mm).

A design optimisation process was adopted by varying the cut-outs geometries (Table 3) in order to ascertain their effect on the structural integrity of the proposed rib design. For all rib cut-outs geometries examined, three different wing ribs were designed: 5 mm web thickness with 10 mm upper and lower caps (model 1), 4 mm web thickness with 8 mm upper and lower caps (model 2) and 3 mm web thickness with 6 mm upper and lower caps (model 3).

Table 3: Dimensions of circular and triangular cut sections

Type	Dimensions (mm)	Spacing (mm)
Left triangle	Base: 105.3 Altitude: 120.5 2 radii of 10	29.5 from rib leading part
Circle 1	Ø 120	Centre 250 from rib leading part
Circle 2 (middle circle)	Ø 130	150 between centre of circle 1 and circle 2
Circle 3	Ø 100	150 between centre of circle 2 and circle 3
Right triangle	Base: 6.89 Altitude: 217.7 2 radii of 10 Vertex angle: 20°	Base 650 from rib leading part

For this research, 7050-T7451 aluminium alloy was used. This alloy is heat treatable and used in various aerospace applications including wing skin, bulkheads and fuselage frames. The mechanical properties of this alloy are shown in Table 4.

Table 4: Material properties of Al 7050-T7451

Parameter	Value
Density	2.83g/cm ³
Young's modulus	2.8·e ¹⁰ Pa
Poisson's ratio	0.33
Bulk modulus	6.9608·e ¹⁰ Pa
Shear modulus	2.6692·e ¹⁰ Pa
Tensile yield strength	2.8·e ⁸ Pa
Compressive yield strength	2.8·e ⁸ Pa
Tensile ultimate strength	5.24·e ⁸ Pa

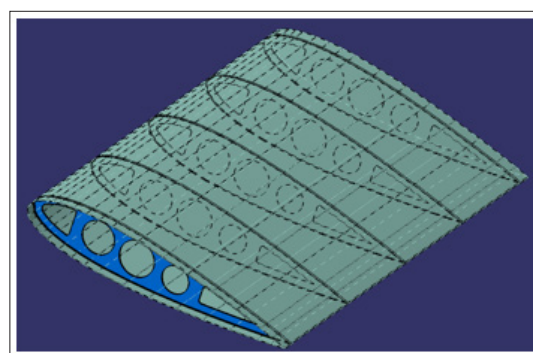


Figure 7: Wing model with 5 ribs

To analyse the wing rib under different loading conditions, a wing rectangle surface with five ribs was designed. The dimensioning of the wing rectangle surface for model 1 is shown in Figure 6.

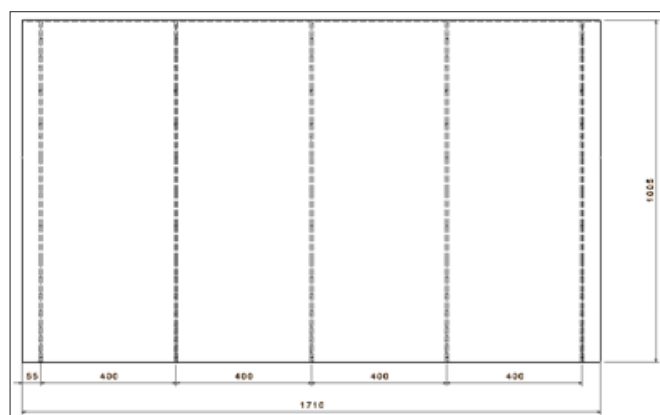


Figure 6: Top view of rectangular wing design with five ribs (dimensions in mm).

During the design process, the optimal spacing of 400 mm between ribs for a rectangular aircraft wing was considered. The dimensions of the rectangle are 1,710 mm x 1,005 mm. For model 1 the distance between the wing root and the first rib is 50 mm, and the distance between the fifth rib and the wing tip is 50 mm for all models. The thickness of the wing skin is 1 mm in all models. The model in Catia is composed of the wing skin and five ribs which are joined together as an assembly.

The sensor locations (SLs) were designed according to the IoT sensor RSL10, a node-to-cloud IoT sensor developed by the company onsemi that can measure temperature, humidity, pressure and acceleration. Its diameter is 30 mm and it has 13 mm thickness. The effective dimensions of the designed sensor housing are 31 mm diameter and it is embedded 2 mm into the rib. The cover is 34.7 mm diameter and 15 mm length. The cover was designed to be assembled and disassembled for maintenance purposes. The idea of sensory integration allows wing ribs with the ability to gather life cycle data when used in harsh/hard-to-reach environments and provides valuable performance monitoring data to improve efficiency.

As a result of modification in thickness, for models 2 and 3 the distances between wing root and first rib were modified during the design process.

Table 5: Model dimensions (mm)

	Model 1	Model 2	Model 3
Distance wing root - Rib 1	50	52	54
Distance wing tip - Rib 5	50	50	50
Wing skin thickness	1	1	1
Embedded sensor depth	2	2	2

The main reason for inserting holes within the cover was to allow heat transfer exchange and the sensory reception of sensing the

environmental magnitudes. In addition, these holes contribute towards the general weight reduction of the component. The sensor locations are shown in Figure 8.

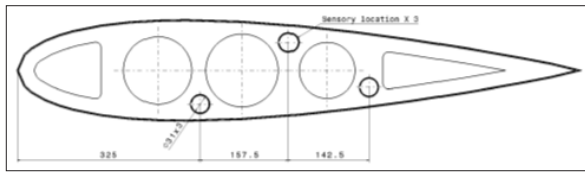


Figure 8: Wing rib with sensor locations (dimensions in mm)

These sensor locations were implemented in the five ribs. Figure 9 shows the dimensions of the sensor housing cover.

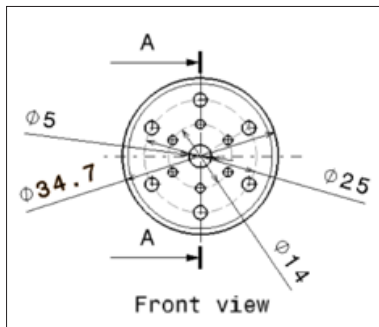


Figure 9: Sensor housing cover dimensions (mm)

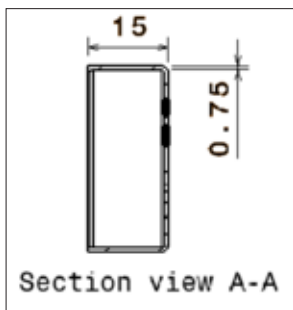


Figure 10: Shows the wing structure with five ribs and the sensor locations.

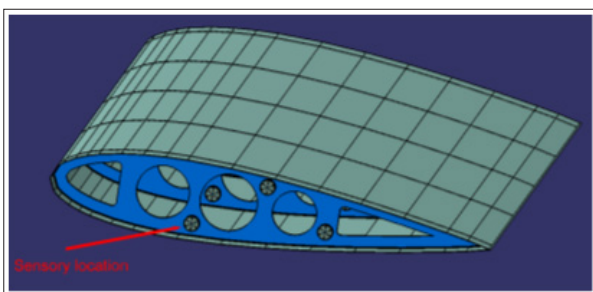


Figure 11: 5-ribs-wing model and sensor locations

Model Analysis

In this work, a wing model was used to perform the simulations, instead of a single rib to facilitate the application of boundary conditions. The design was imported to Ansys and meshed with elements of tetrahedral order for the wing skin and ribs. The ribs were meshed by varying the element size to refine the number of nodes and elements to improve the quality index. In this work, mesh suitability is assessed using an element quality index which provides a value between 0 and 1. The focus is on analysing the ribs rather than the wing skin. The ribs element size was modified to compare the total deformation and the average element quality.

Figure 12 shows the mesh for the wing model without SL.

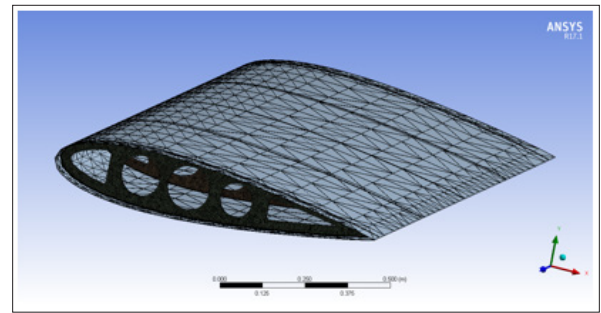


Figure 12: Mesh generation without SL (5 mm rib thickness)

This tetrahedron mesh is composed of 626,788 nodes and 355,551 elements, with rib element size of 4 mm. The mesh with SL is also tetrahedron, it has 726,628 nodes and 406,016 elements, with rib element size of 4 mm.

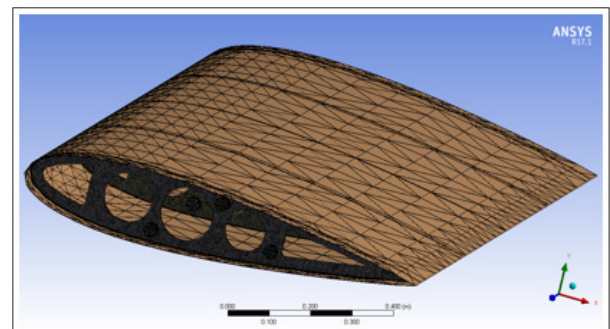


Figure 13: Mesh generation with SL (5 mm rib thickness)

The lift force can be estimated as the product between mass and the gravitational acceleration:

$$F_{Boeing} = m_{Boeing} \cdot g = 183,500 \text{ kg} \cdot 9.81 \frac{\text{m}}{\text{s}^2} = 1,800,135 \text{ N} \quad (1)$$

For each wing, the pressure applied to the upper wing surface is:

$$P_{Boeing,wing} = \frac{F_{Boeing,wing}}{S_{Boeing,wing}} \quad (2)$$

where $S_{Boeing,wing}$ is the upper wing surface, which is 511 m². Taking into account that one aircraft wing must withstand half of the total aircraft weight, the pressure is:

$$P_{Boeing,wing} = \frac{F_{Boeing,wing}}{S_{Boeing,wing}} = \frac{1}{2} \cdot \frac{F_{Boeing}}{S_{Boeing,wing}} \quad (3)$$

For the simulation model, the pressure is maintained as in the Boeing aircraft to keep the relation force/surface constant. Thus,

$$P_{model,wing} = P_{Boeing,wing} \quad (4)$$

Besides, the pressure in case of the model can be expressed as:

$$P_{model,wing} = \frac{F_{model,wing}}{S_{model,wing}} \quad (5)$$

From the Catia design, the upper surface of the wing is $S_{model,wing} = 1.7845 \text{ m}^2$, which is calculated from the total wing surface 3.569

m². The force for the boundary condition in the simulation model can be calculated as:

$$F_{model,wing} = P_{model,wing} \cdot S_{model,wing} = P_{Boeing,wing} \cdot S_{model,wing} = \frac{1}{2} \cdot F_{Boeing} \cdot S_{model,wing} \quad (6)$$

$$F_{model,wing} = \frac{1}{2} \cdot F_{Boeing} \cdot S_{model,wing} = \frac{1}{2} \cdot 1,800,135 \text{ N} \cdot 1.7845 \text{ m}^2 = 3143.2 \text{ N} \quad (7)$$

The secondary boundary condition for the simulation model is to fix the wing root to the fuselage, as in real aircrafts. The figure below shows the boundary conditions for the wing model: applied distributed force and fixed support at the wing root. They will be applied to the models with and without sensory locations.

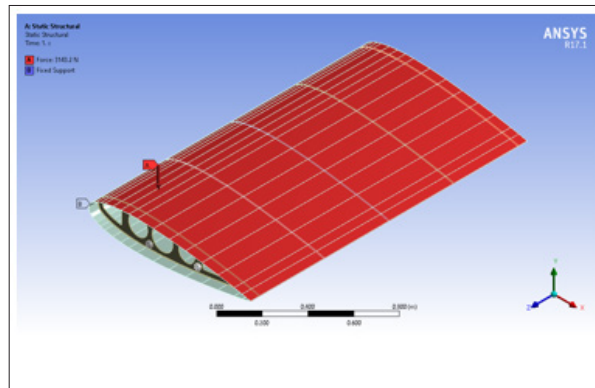


Figure 14: Boundary conditions

In the following subsections, the simulation results for the three wing rib models will be explained: 5 mm web thickness with 10 mm upper and lower caps, 4 mm web thickness with 8 mm upper and lower caps, and 3 mm web thickness with 6 mm upper and lower caps. The first wing rib geometry was designed considering 5 mm thickness and 10 mm for the caps. The others two rib

geometries were designed to keep the ratio $\frac{\text{rib thickness}}{\text{lower and upper caps}}$ constant. Besides, each model was simulated with and without

sensory cut-outs. The two boundary conditions explained in the above section are applied: vertical distributed force (3143.2 N) and fixed wing root. In the following, the ribs will be named as first rib (found at the wing root), second rib, third rib, fourth rib, and fifth rib (at the wing tip). For each rib wing model, three cases were analysed: without sensory location (SL), with SL and covers, with SL and without covers. These cases will be named as “variant 1”, variant 2” and “variant 3”, respectively. To check the most suitable solution for embedded sensory capability for AM processes considering deformation and stress distribution, the analysis was also done with and without covers.

Five-Ribs Wing Model 1: Rib with 5 mm thickness and 10 mm upper and lower caps

Variant 1: Without SL

The rib element size was varied between 10 mm and 3.3 mm in order to optimise the ribs meshing. Considering the total deformation, the convergence point was found for rib element size of 4.1 mm with 586,613 nodes and 331,801 elements. For this element size, the average element quality is 0.70624. Figure 15 shows the element quality graph for this model. The first and second bars correspond respectively to the wing skin and the elements located between both wing skin and ribs. Since variation of element size for meshing the skin was not considered, these elements present lower element quality. The other bars correspond to the ribs for which the element size is 4.1 mm.

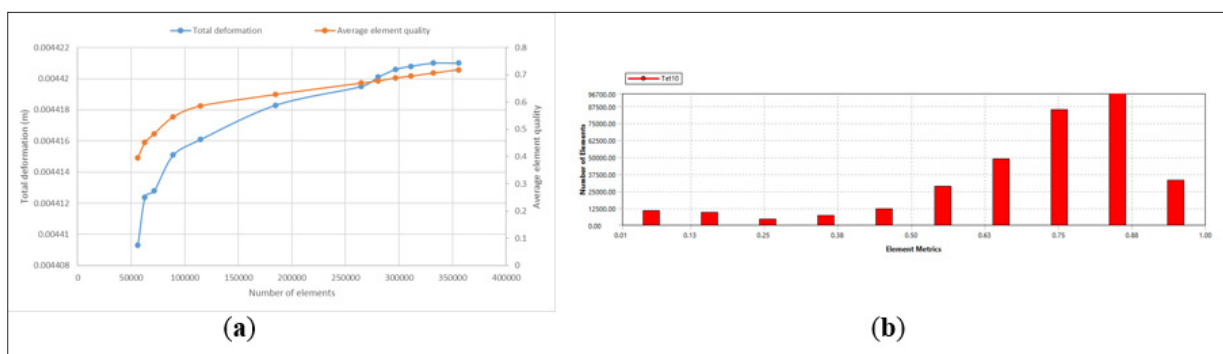


Figure 15: (a) Total deformation and average element quality; (b) Element quality graph.

Figure 16 shows the total deformation for the entire wing model. The minimum deformation occurs at the wing root, while its maximum value (4.421 mm) is found at the wing tip. This result is plausible in accordance with the applied boundary conditions. Since the maximum deformation occurs at the wing tip, the fifth rib is chosen to be analysed. Its maximum deformation is found at the trailing edge, while the minimum value is at the leading edge.

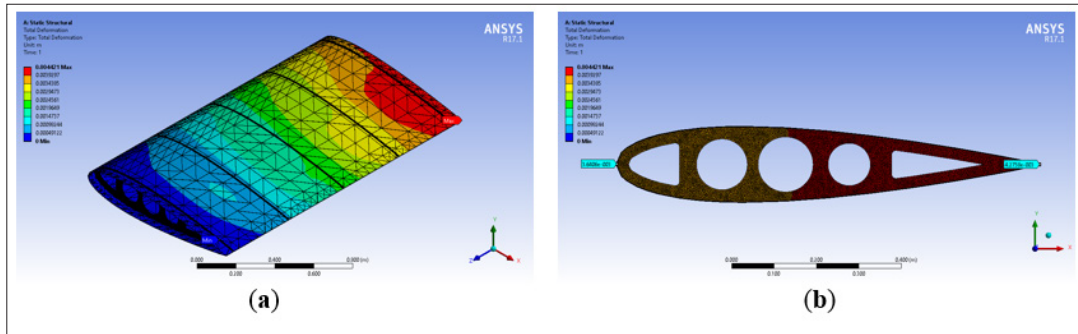


Figure 16: Total deformation: (a) Wing model 1 - variant 1; (b) Fifth rib.

The equivalent von-Mises stress was also obtained. Within the wing, the maximum stress occurs in the first rib, and the minimum in the wing skin. Since the wing root is fixed, the applied force provokes that the first rib suffers from the maximum stress. Within the first rib, the maximum stress is found at the trailing edge. The stress is concentrated around circles 2 and 3, and the right triangle.

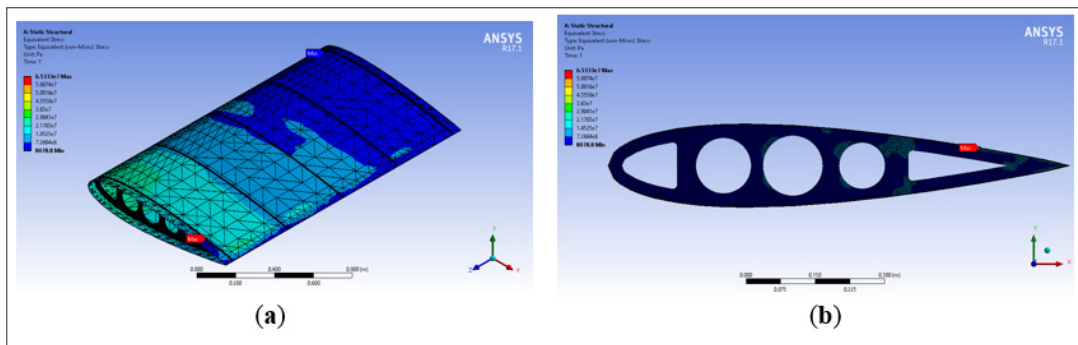


Figure 17: Equivalent von-Mises stress: (a) Wing model 1 - variant 1; (b) First rib.

Variant 2: SL with Covers

Each rib has three sensory locations respectively with covers. In the following sections, they will be referred as left, middle and right. Their location has been selected considering the most affected area by total deformation and stress before inserting sensory locations (variant 1). Besides, a minimum of three IoT sensors devices are implemented to build a wireless sensor network (WSN). Each IoT sensor device can collect data from its environment, and they can communicate with each other to transmit data that can be analysed for different purposes, such as predictive maintenance. The scope here is to enhance the capability of wing ribs by embedding IoT sensors into AM processes to prolong the lifecycle of aircraft wings when used in harsh environments. The smart rib can be used in an Industry 4.0 ecosystem for collecting sensory data for aircraft health monitoring and predictive maintenance. The implemented IoT sensors RSL10 in this work can measure temperature, humidity, pressure and acceleration, which will be collected, analysed and converted into information to achieve a data-driven predictive maintenance-based system.

The analysis for “SL with cover” was done considering ribs element size from 10 mm to 3.5 mm. The results show that the maximum total deformation oscillates with certain damping, and it converges around a constant value.

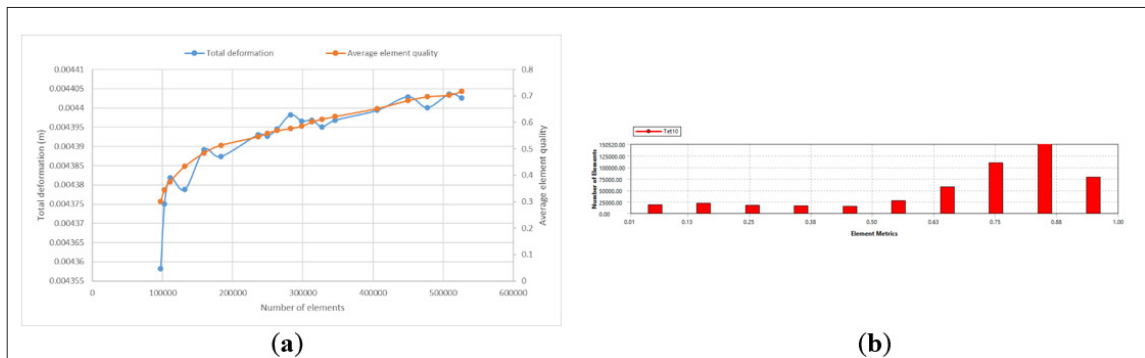


Figure 18: (a) Total deformation and average element quality; (b) Element quality graph

In this case, the convergence point was selected for rib element size of 3.6 mm as the most suitable and representative. It has 900,343 nodes and 508,686 elements. For this element size, the average element quality is 0.70359.

As in variant 1, the rib wing model variant 2 shows that the minimum deformation occurs at the wing root, while its maximum value is found at the wing tip. Now, the maximum value for the total deformation has been decreased as a result of the embedded SL with covers (4.4 mm). Considering the total deformation, the most affected rib is the fifth one, whose value for the maximum deformation is located at the trailing edge, which is also less than in variant 1.

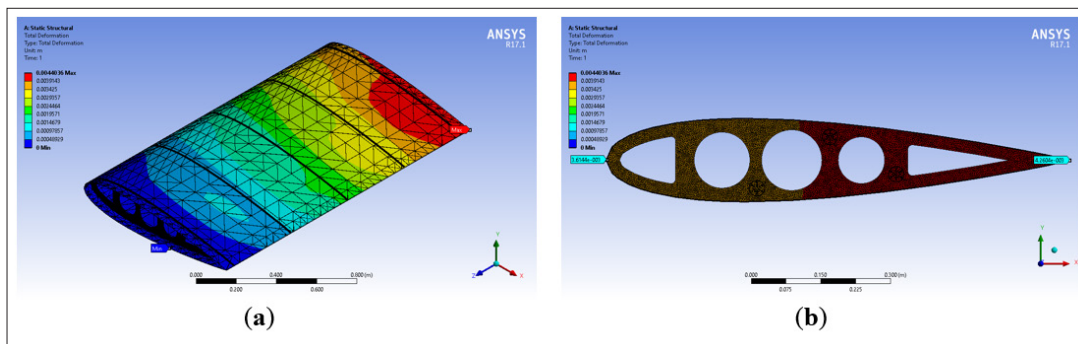


Figure 19: Total deformation: (a) Wing model 1 - variant 2; (b) Fifth rib

The maximum equivalent von-Mises stress is greater than the five ribs wing model variant 1. However, the stress is concentrated around a specific area in the fourth rib. Figure 20 shows the stress distribution for the entire wing in logarithmic scale for better understanding.

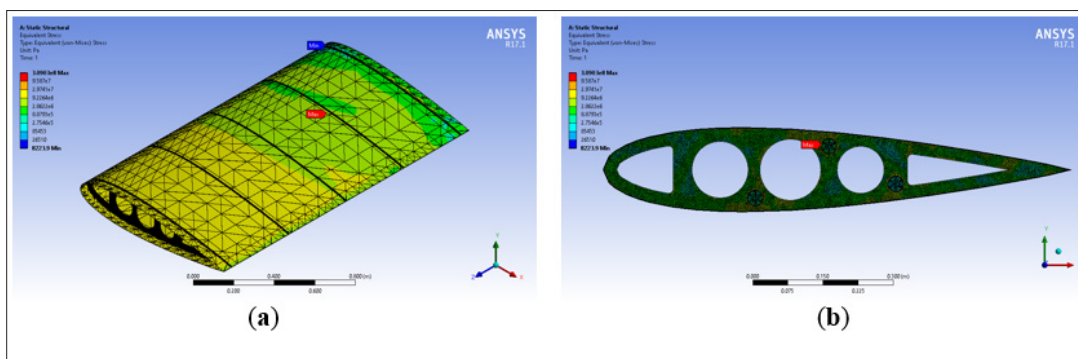


Figure 20: Equivalent von-Mises stress: (a) Wing model 1 - variant 2; (b) Fourth rib

The most affected rib by the stress is the fourth one. For this rib, the maximum stress is at the sensory location located between circles 2 and 3. By analysing this area of the fourth rib, the maximum stress concentration is found around the middle sensory location. Figure 21 shows a detail of the stress distribution for this location and a detail of the sensory location edge at which the maximum stress occurs.

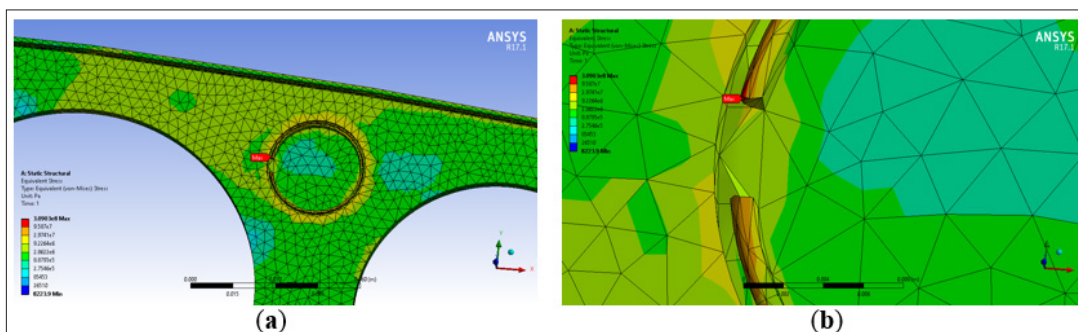


Figure 21: Equivalent von-Mises stress: (a) Left sensory cover of fourth rib 2; (b) Detailed view of maximum stress location

Variant 3: SL without Covers

The analysis for variant 3 was done considering ribs element size from 10 mm to 4 mm. The convergence point for the maximum total deformation was found for rib element size of 4.2 mm with 586,048 nodes and 328,231 elements.

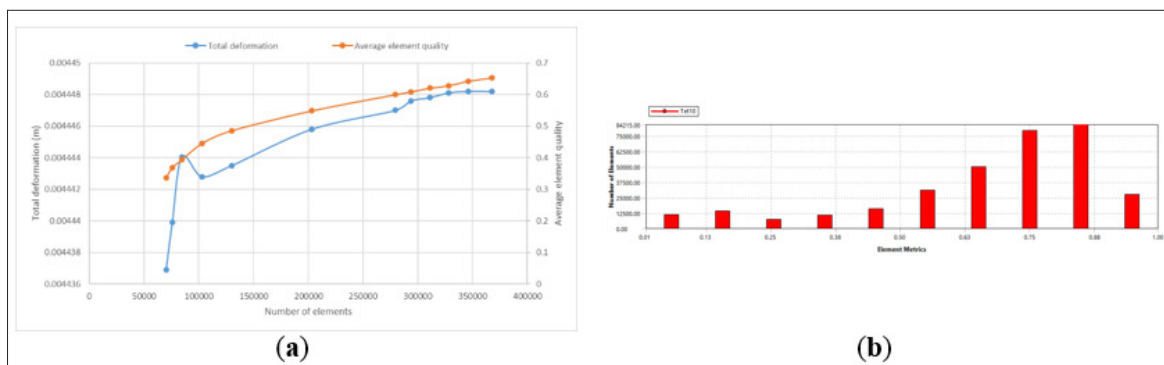


Figure 22: (a) Total deformation and average element quality; (b) Element quality graph.

For this element size, the average element quality is 0.62829. The first two bars of the quality element graph correspond to the wing skin and the elements located between both wing skin and ribs. The other bars correspond to the ribs for which the element size is 4.2 mm.

The minimum deformation occurs at the wing root, while its maximum value (4.45 mm) is found at the wing tip. The fifth rib presents its maximum deformation at the trailing edge, and its minimum value is at the leading edge.

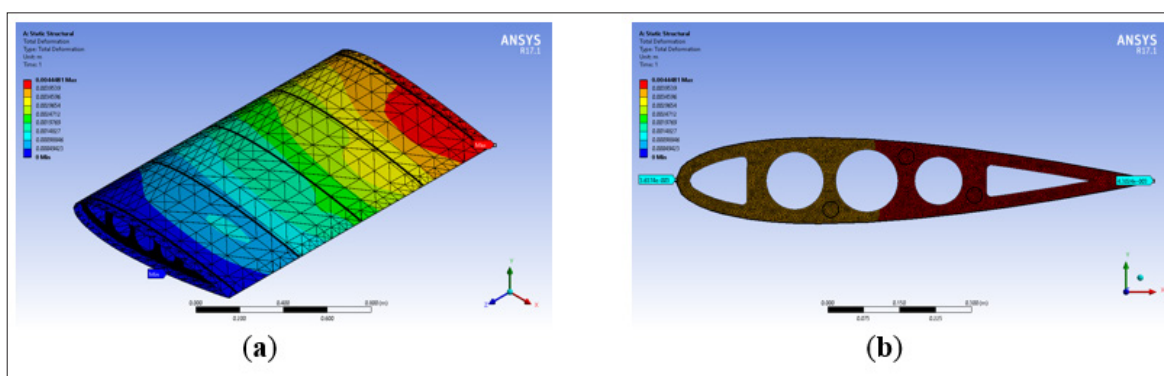


Figure 23: Total deformation: (a) Wing model 1 - variant 3; (b) Fifth rib.

The stress graph shows that the maximum stress is at the first rib, and its minimum value is at the third. The results show that for variant 3 the maximum stress is at the leading edge of the first rib. The stress is concentrated around the rib circles and the SL.

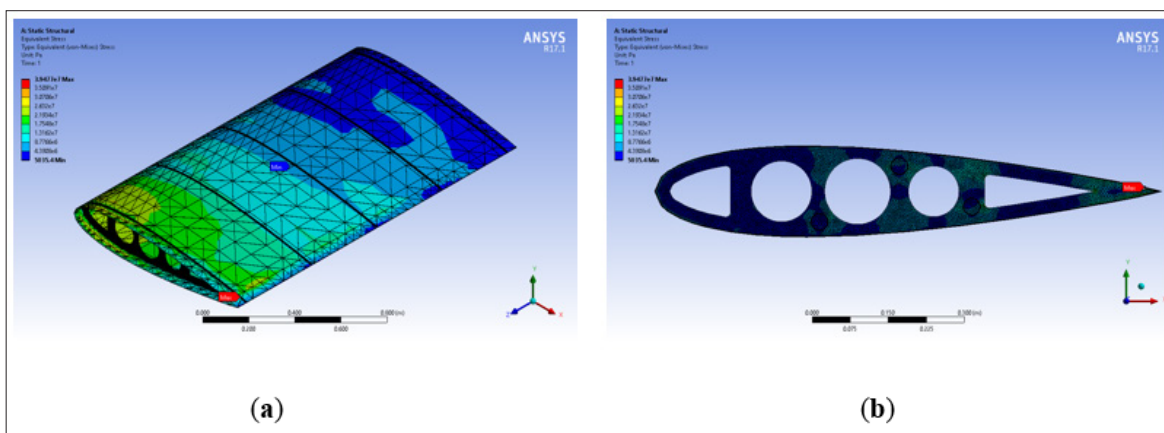


Figure 24: Equivalent von-Mises stress: (a) Wing model 1 - variant 3; (b) First rib.

Five-Ribs Wing Model 2: Rib with 4 mm thickness and 8 mm upper and lower caps

The second geometry was designed considering 4 mm thickness with 8 mm upper and lower caps. Three cases were analysed: without SL (variant 1), with SL and covers (variant 2), with SL and without covers (variant 3).

Variant 1: Without SL

The analysis for variant 1 was done considering ribs element size from 10 mm to 3.8 mm. The convergence point for the maximum total deformation was found for rib element size of 3.9 mm with 546,303 nodes and 296,746 elements.

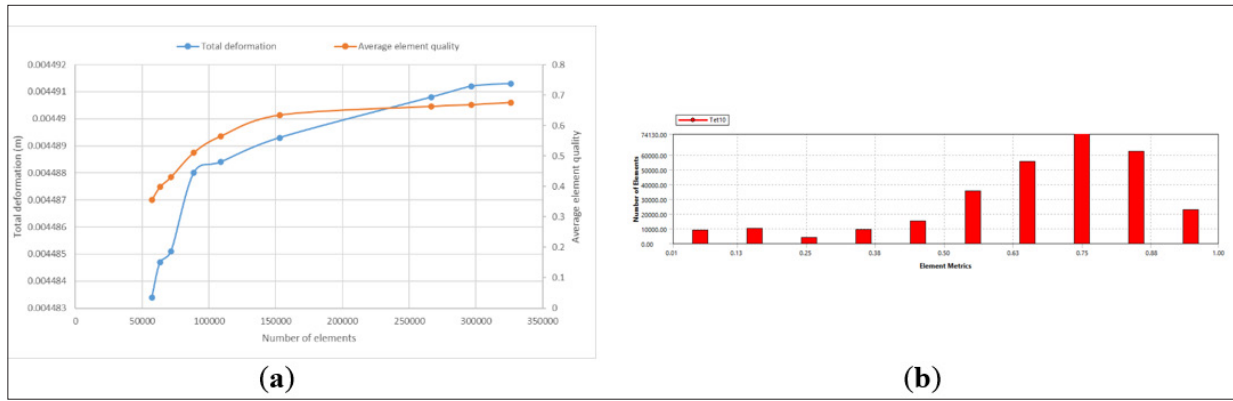


Figure 25: (a) Total deformation and average element quality; (b) Element quality graph.

For 3.9 mm element size, the average element quality is 0.66815. The first two bars of the quality element graph correspond to the elements that belong to the wing skin and those located between both wing skin and ribs. The other bars correspond to the ribs for which the element size is 3.9 mm.

The maximum and minimum values of total deformation are located on the wing surface, and the most affected rib by the deformation is the fifth one. For the fifth rib, the minimum deformation is at the leading edge, and the maximum value at the trailing edge.

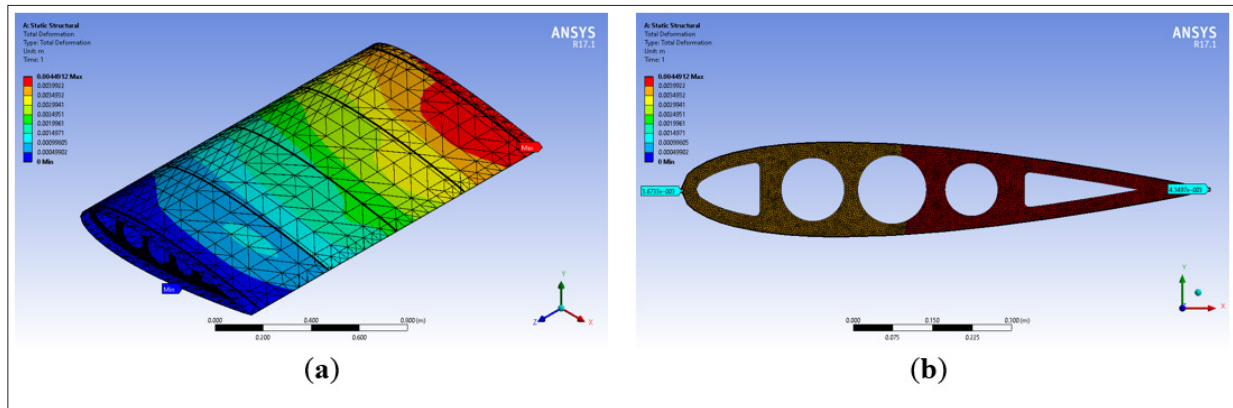


Figure 26: Total deformation: (a) Wing model 2 - variant 1; (b) Fifth rib.

The minimum stress is at the wing tip surface, while the maximum value occurs at the first rib. Considering the first rib, it is found that the maximum stress (45.25 MPa) is at the trailing edge. The stress is concentrated around circle 2, circle 3 and the right triangle.

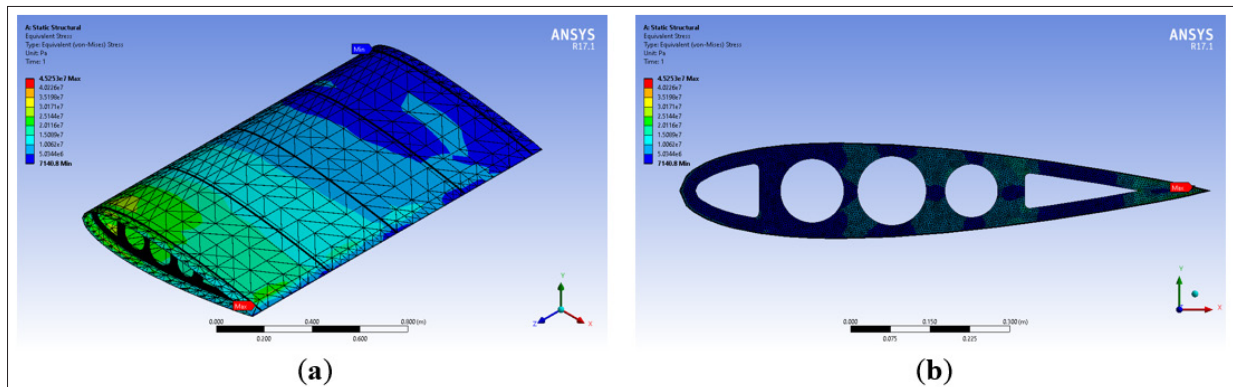


Figure 27: Equivalent von-Mises stress: (a) Wing model 2 - variant 1; (b) First rib

VARIANT 2: SL with Covers

This rib model was analysed with SL and covers. The ribs element size was varied from 10 mm to 4 mm. The convergence point for the maximum total deformation was found for rib element size of 4.5 mm with 465,843 nodes and 238,011 elements.

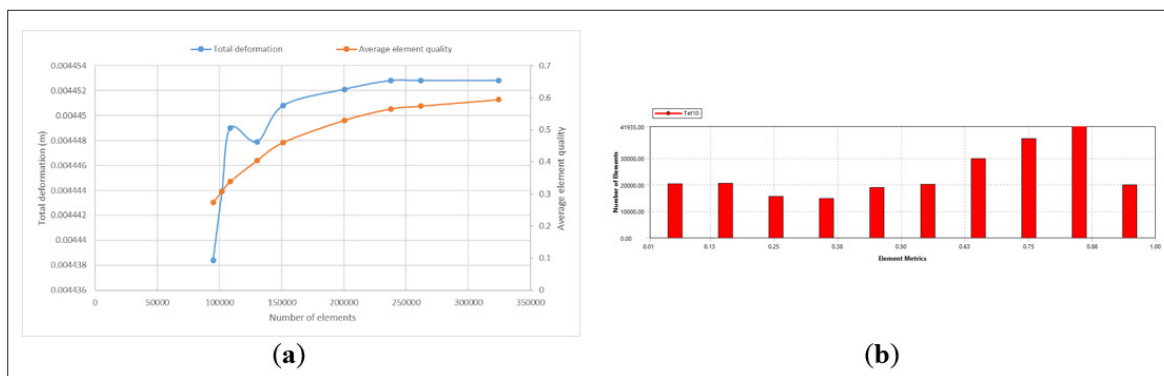


Figure 28: (a) Total deformation and average element quality; (b) Element quality graph.

For 4.5 mm element size, the average element quality is 0.56557. The first two bars of the quality element graph correspond to the elements that belong to the wing skin and those located between both wing skin and ribs. The other bars correspond to the ribs for which the element size is 4.5 mm.

For this wing model, the deformation behaves as in the other cases: the minimum at the wing root and the maximum at the wing tip, both on the wing surface. Figure 29 shows the total deformation for the fifth rib. Its minimum deformation is at the leading edge, while the maximum value is at the trailing edge, as in the previous cases.

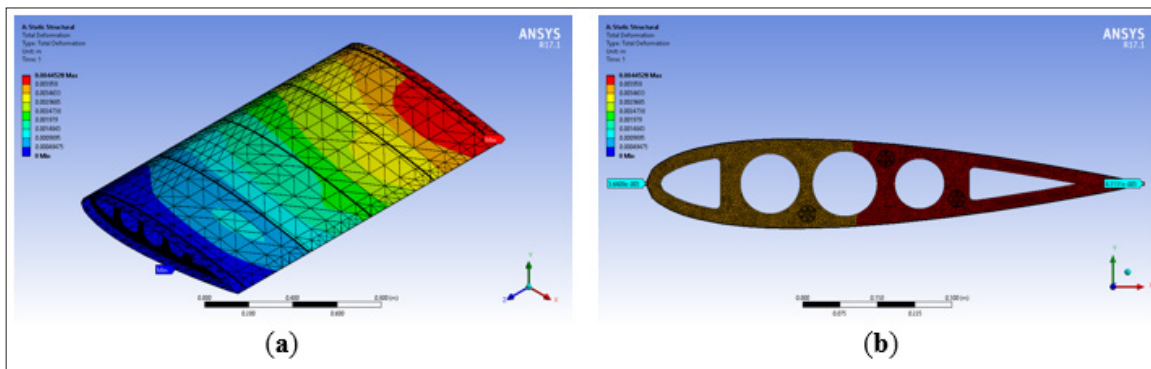


Figure 29: Total deformation: (a) Wing model 2 - variant 2; (b) Fifth rib.

The stress distribution in this case has been displayed in logarithmic scale to achieve better understanding of the differences between the wing regions. The minimum stress occurs on the wing surface close to the wing tip, and the maximum value occurs on the right sensor's cover of fifth rib.

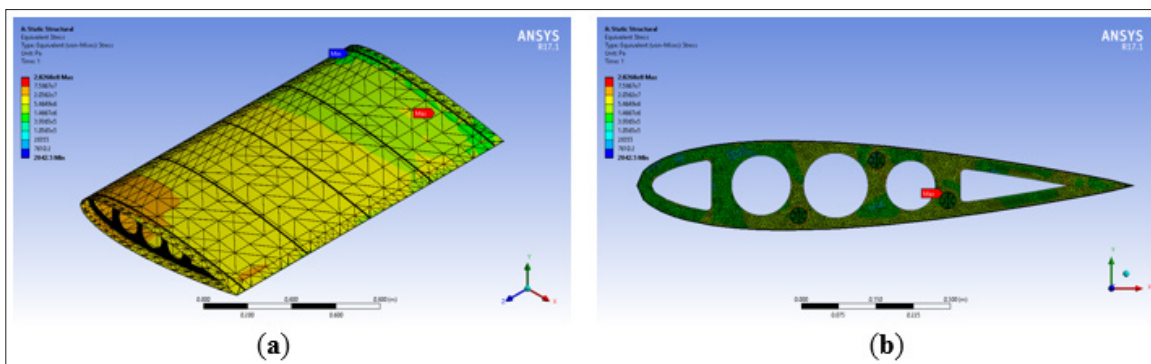


Figure 30: Equivalent von-Mises stress: (a) Wing model 2 - variant 2; (b) First rib.

The stress distribution for the fifth rib has been also displayed in logarithmic scale to achieve a detailed representation. The picture below shows the stress distribution of the right sensory cover. The maximum stress is around the edge of the cover.

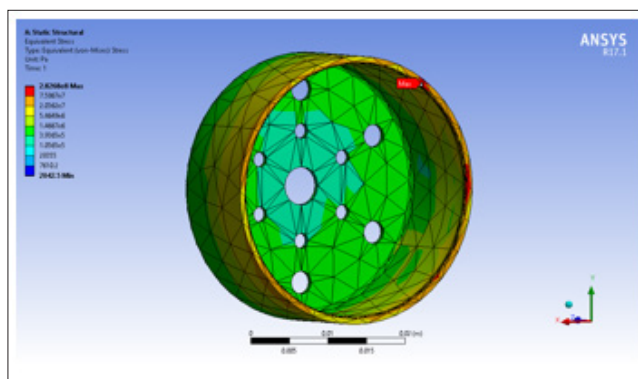


Figure 31: Equivalent von-Mises stress: right sensory cover of fifth rib

Variant 3: SL without Covers

The rib element size was varied between 10 mm and 3.8 mm in order to optimise the ribs meshing. Considering the total deformation, the convergence point was found for rib element size of 3.9 mm with 582,493 nodes and 315,561 elements.

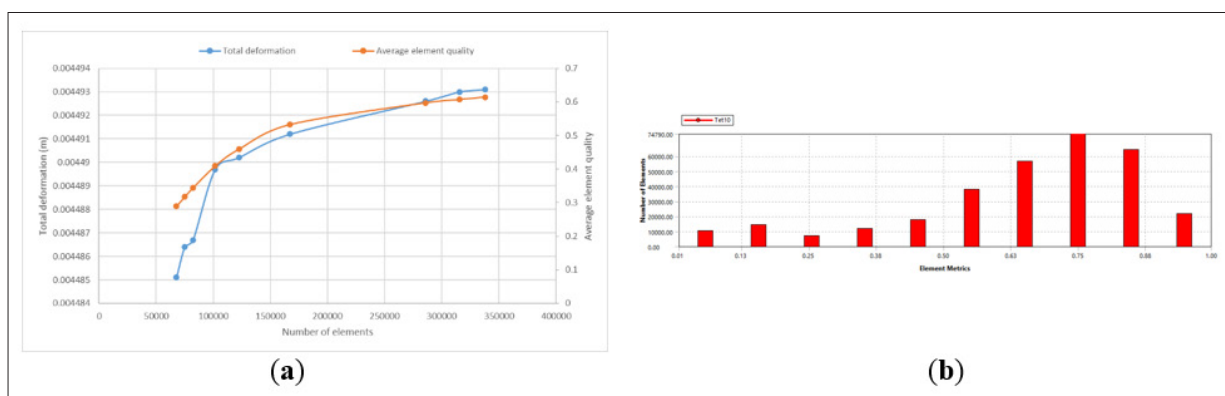


Figure 32: (a) Total deformation and average element quality; (b) Element quality graph.

For this element size, the average element quality is 0.60709. The first and second bars correspond respectively to the wing skin and the elements located between both wing skin and ribs. Since variation of element size for meshing the skin was not considered, its elements present lower element quality. The other bars correspond to the ribs for which the element size is 3.9 mm.

The analysis of the deformation is similar to the previous cases: the maximum deformation is on the surface at the wing tip, and the minimum value on the surface at the wing root. Figure 33 gives an overview of the total deformation for the fifth rib. Its maximum deformation is at the trailing edge, and the minimum vale at the leading edge.

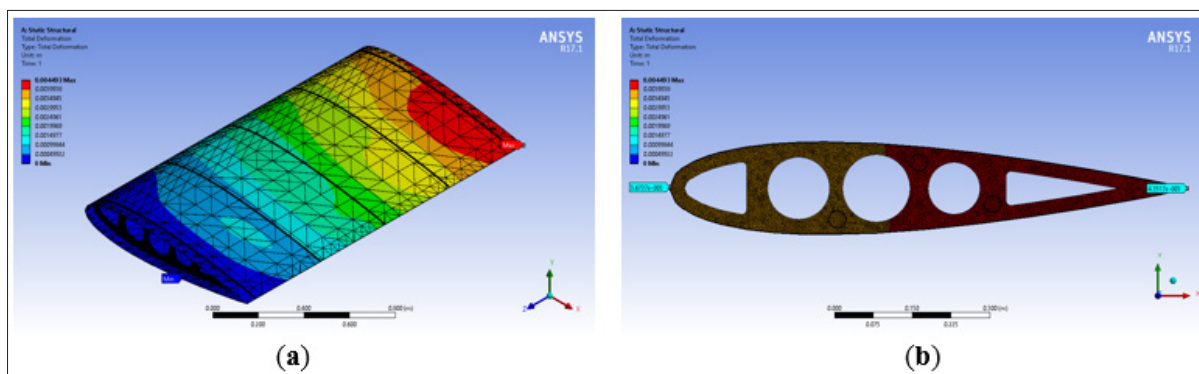


Figure 33: Total deformation: (a) Wing model 2 - variant 3; (b) Fifth rib

The stress distribution shows that the minimum stress is at the wing surface close to the wing tip, and the first rib suffers from the maximum stress. Within the first rib, the maximum stress is found at the trailing edge.

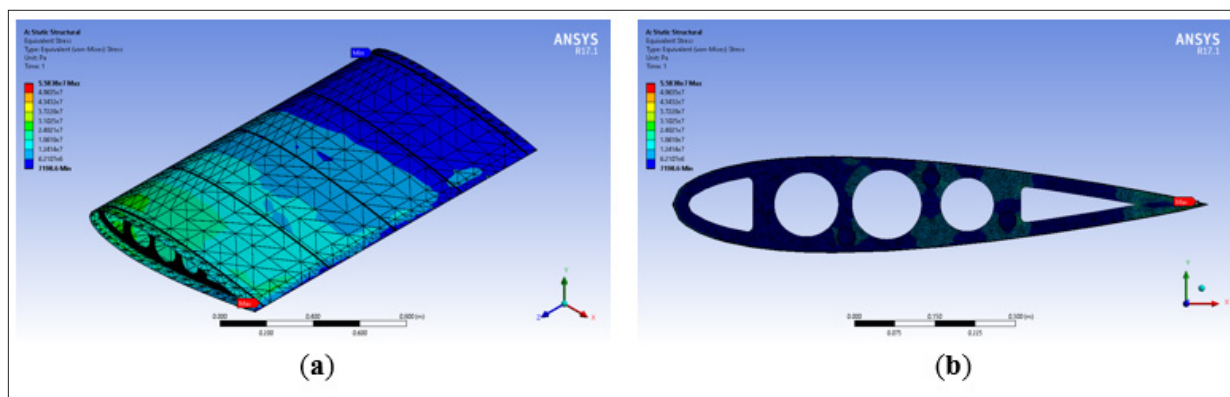


Figure 34: Equivalent von-Mises stress: (a) Wing model 2 - variant 2; (b) First rib

Five-Ribs Wing Model 3: Rib with 3 mm thickness and 6 mm upper and lower caps

The third model that was simulated consisted of 3 mm thickness with 6 mm upper and lower caps. The same process is followed: analysis without SL (variant 1), with SL and covers (variant 2), and with SL without covers (variant 3).

Variant 1: Without SL

This rib model was analysed without SL. The ribs element size was varied from 10 mm to 3.1 mm. The convergence point for the maximum total deformation was found for rib element size of 3.2 mm with 664,678 nodes and 348,916 elements.

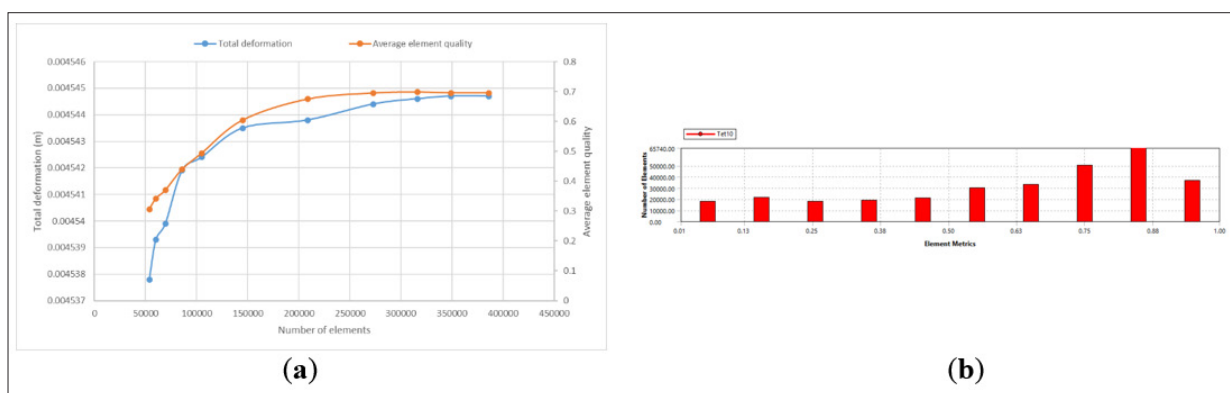


Figure 35: (a) Total deformation and average element quality; (b) Element quality graph

For 3.2 mm element size, the average element quality is 0.69557. The first two bars of the quality element graph correspond to the elements that belong to the wing skin and those located between both wing skin and ribs. The other bars correspond to the ribs for which the element size is 3.2 mm. Like the previous wing rib models, within the fifth rib the maximum deformation is at the trailing edge, and the minimum value at the leading edge.

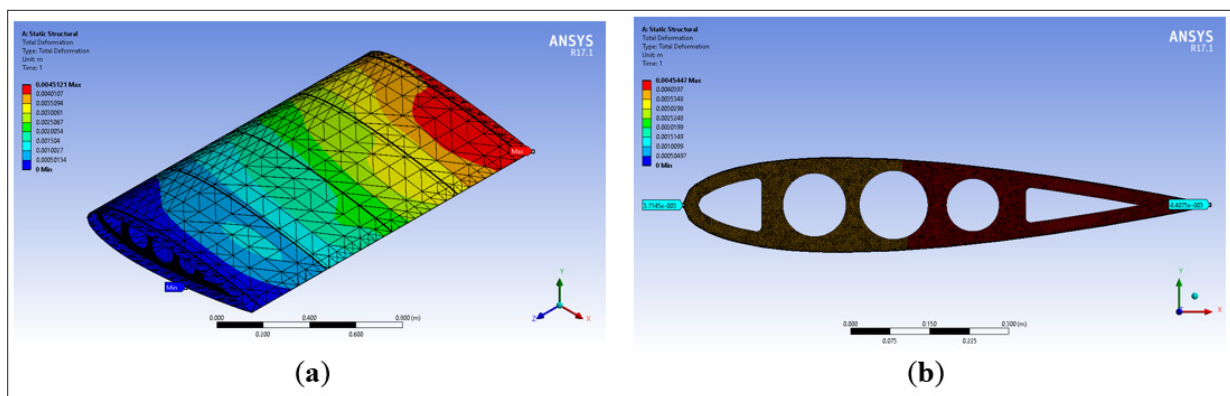


Figure 36: Total deformation: (a) Wing model 3 - variant 1; (b) Fifth rib

The stress distribution shows that the maximum value is on the first rib, and the minimum value on the wing surface close to the wing tip. The figure shows the stress distribution of the first rib. It is concentrated around the circles and the right triangle, and the maximum stress is at the trailing edge.

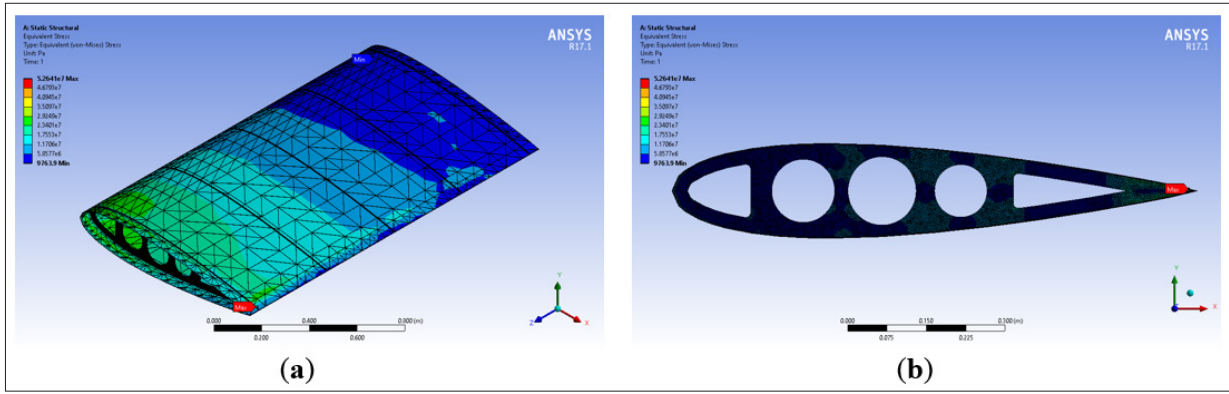


Figure 37: Equivalent von-Mises stress: (a) Wing model 3 - variant 1; (b) First rib.

VARIANT 2: SL with Covers

This next rib model was analysed with SL and covers. The ribs element size was varied from 10 mm to 3.6 mm. The convergence point for the maximum total deformation was found for rib element size of 3.6 mm with 615,443 nodes and 311,261 elements.

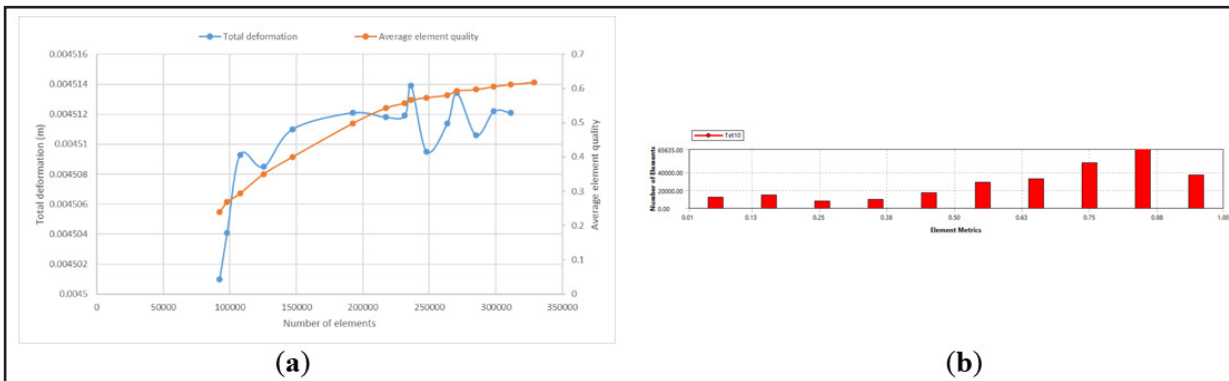


Figure 38: (a) Total deformation and average element quality; (b) Element quality graph

As the first rib wing model (rib thickness 5 mm with 10 mm upper and lower caps) variant 2, the maximum total deformation oscillates with certain damping. The curve converges around a constant value. The most representative rib element size was selected for 3.5 mm, with average element quality 0.61773. The first two bars of the quality element graph correspond to the elements that belong to the wing skin and those located between both wing skin and ribs. The other bars correspond to the ribs for which the element size is 3.5 mm. The total deformation distribution shows that the minimum value is on the surface of the wing root, whilst the maximum deformation occurs at the wing tip. Within the fifth rib, the results are similar as in the previous cases. The maximum deformation for this rib is at the trailing edge, and the minimum value at the leading edge.

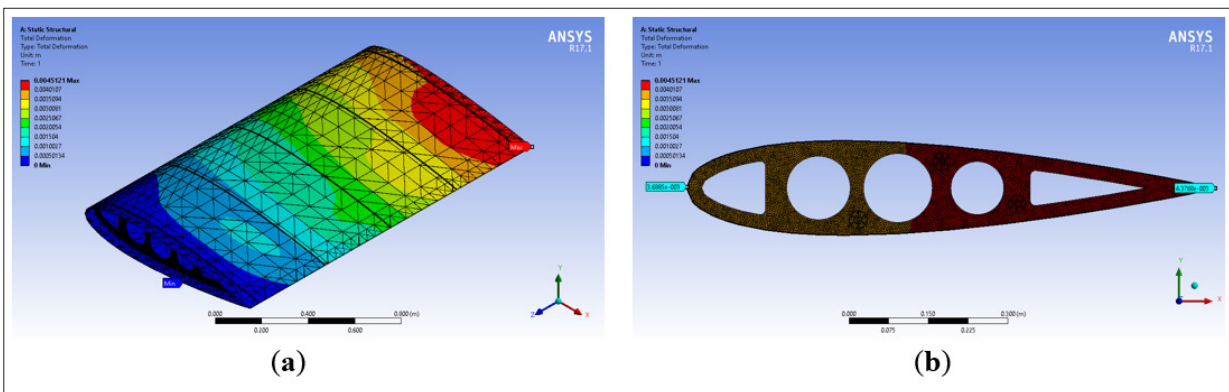


Figure 39: Total deformation: (a) Wing model 3 - variant 2; (b) Fifth rib.

The equivalent stress distribution shows now that the maximum stress is located on the fourth rib, and the minimum value is close to the wing tip.

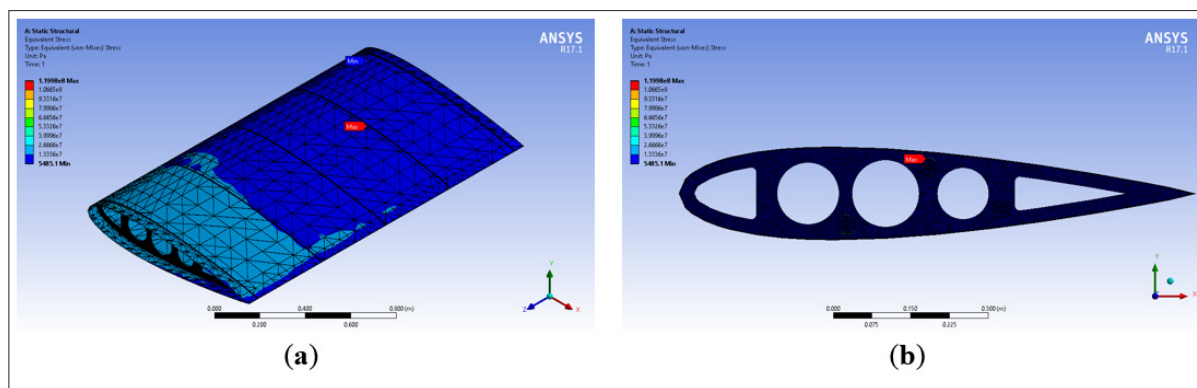


Figure 40: Equivalent von-Mises stress: (a) Wing model 3 - variant 2; (b) Fourth rib.

Considering the fourth rib in detail, the maximum deformation is found at the middle SL, between circles 2 and 3. Figure 41 shows the stress distribution around the middle SL of the fourth rib in detail. Compared to the previous analysed geometries for variant 2, the stress concentration here is found around the SL, while the other two cases showed the maximum stress on the sensory covers.

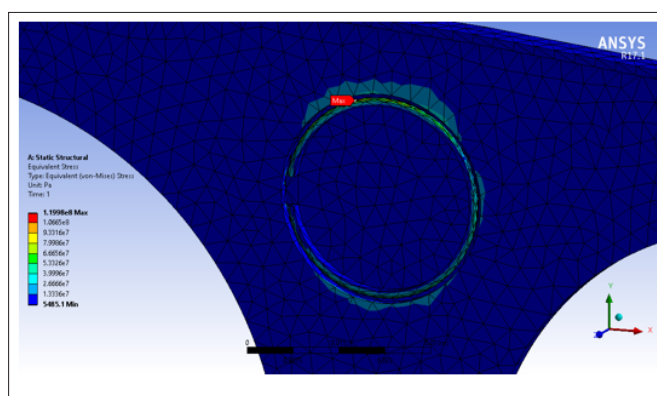


Figure 41: Equivalent von-Mises stress: middle SL of fourth rib

Variant 3: SL without Cover

For the last case, the rib element size was varied between 10 mm and 3.4 mm in order to optimise the ribs meshing. Considering the total deformation, the convergence point was found for rib element size of 3.6 mm with 538,073 nodes and 272,666 elements.

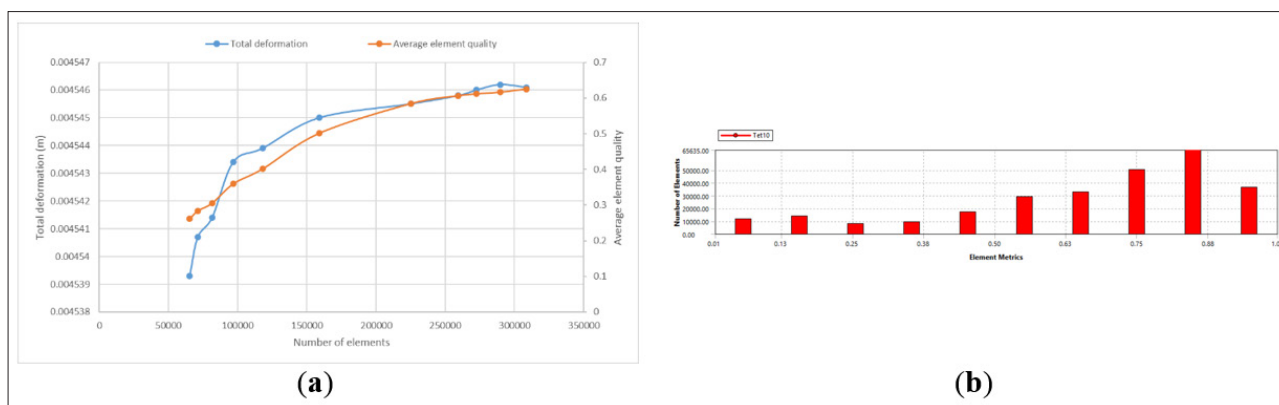


Figure 42: (a) Total deformation and average element quality; (b) Element quality graph

For this element size, the average element quality is 0.61175. The first and second bars correspond respectively to the wing skin and the elements located between both wing skin and ribs. Since variation of element size for meshing the skin was not considered, it presents lower element quality. The other bars correspond to the ribs for which the element size is 3.6 mm.

As in all previous wing rib models, the minimum deformation is at the wing root, and the maximum deformation occurs at the wing tip. The total deformation of the fifth rib shows that the minimum and maximum values are found respectively at the leading and trailing edge. Figure 43 shows the total deformation of the fifth rib.

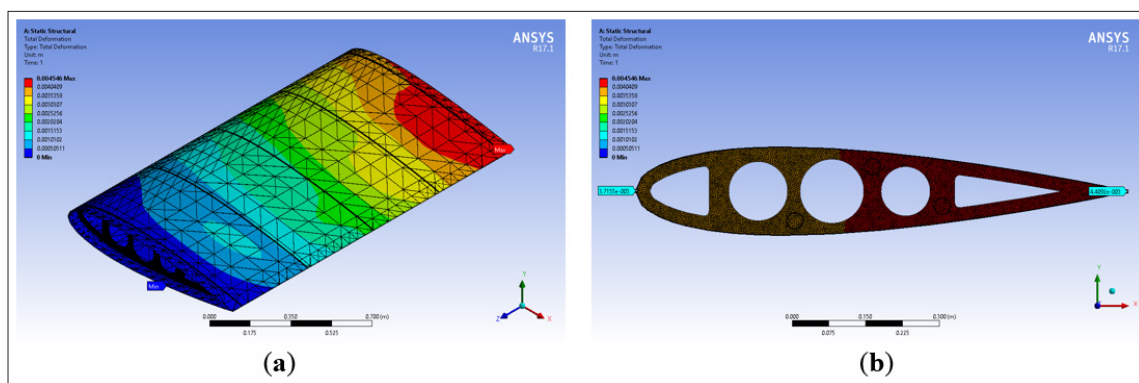


Figure 43: Total deformation: (a) Wing model 3 - variant 3; (b) Fifth rib

The stress distribution in this case gives the maximum value on the first rib, but it is less compared to the previous cases of variant 3. Figure below shows the detailed stress distribution on the first rib, where the stress is concentrated around the circles and trailing edge.

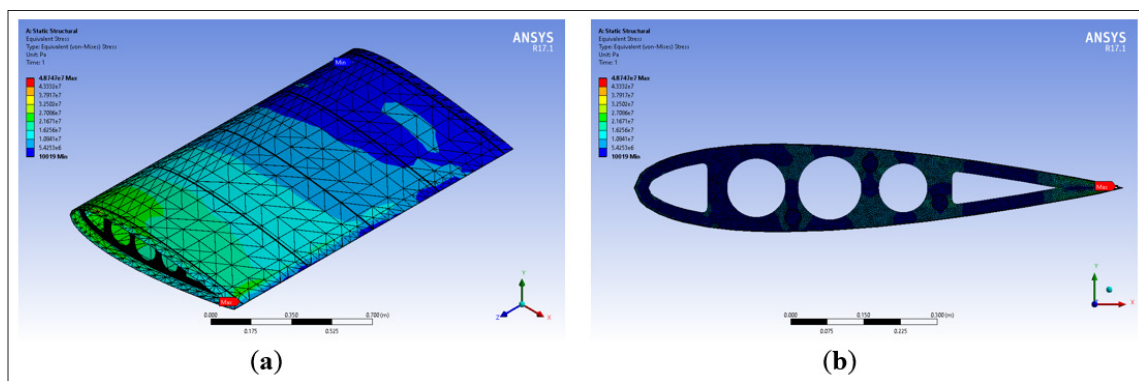


Figure 44: Equivalent von-Mises stress: (a) Wing model 3 - variant 2; (b) First rib

Results and Discussion

In this work, the NACA 0018 profile was selected to design an aircraft wing rib suitable for DfAM. In addition, a design optimisation process was adopted by varying the cut-outs geometries in order to ascertain their effect on the structural integrity of the proposed rib design. Three different wing rib models were designed and analysed: 5 mm rib thickness with 10 mm upper and lower caps (model 1), 4 mm rib thickness with 8 mm upper and lower caps (model 2) and 3 mm rib thickness with 6 mm upper and lower caps (model 3). The material selected was Al 7050-T7451, which is suitable for SLM process. The first boundary condition for the wing models was to fix the wing root as in real aircraft wings that are fixed to the fuselage. For each wing model three cases were analysed: “without SL” (variant 1), “with SL and covers” (variant 2), and “with SL without covers” (variant 3). For each case, the rib element size was varied to obtain the convergence value for the total deformation. The scope was to determine stress and deformation under operating conditions and to know what influence the sensor location has on the stress distribution of wing ribs. In addition, stress and deformation were analysed considering rib thickness.

The analysis of model 1 shows that the total deformation is higher for variant 3 compared to variant 2, that shows less deformation. Variants 1 and 2 show a clear convergence to a constant value for the deformation. Variant 3 shows that the deformation oscillates, but the convergence value can be obtained.

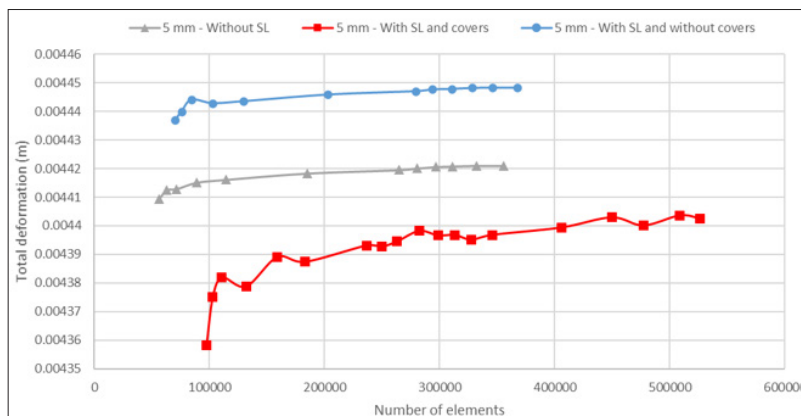


Figure 45: Total deformation for model 1

For the three cases of model 1 the maximum total deformation was located on the wing surface close to the wing tip. Considering variant 1 as reference, the total deformation was decreased by 0.39 % for variant 2, while in variant 3 the deformation was increased by 0.61 %. These results showed that there was no significant difference regarding deformation between the three variants for wing rib model 1. The stress distribution showed that the maximum equivalent stress was increased by around 470 % for variant 2 compared to the maximum stress for variant 3 that decreased by 39 %. Moreover, for variants 1 and 3 the maximum stress occurred on the first rib, and in variant 2 it was on the middle SL of rib 4.

Table 6: Summary for model 1 – rib with 5 mm web thickness

	Variant 1	Variant 2	Variant 3
Maximum deformation (mm)	4.4210	4.4036	4.4481
Deformation difference (%)	-	-0.39	0.61
Location	Wing tip	Wing tip	Wing tip
Maximum stress (MPa)	65.33	309.03	39.48
Stress difference (%)	-	473.01	-39.58
Location	Rib 1	Middle SL rib 4	Rib 1

The wing rib model 2 presented differences to wing rib model 1. For model 2, the maximum deformation was for variant 3, whilst the minimum deformation was found for variant 2. In this model, the deformation difference between variants 1 and 3 is less than in the wing rib model 1. Besides, the curve of the total deformation for variant 2 did not oscillate. The location of the maximum deformation is on the wing surface close to the wing tip.

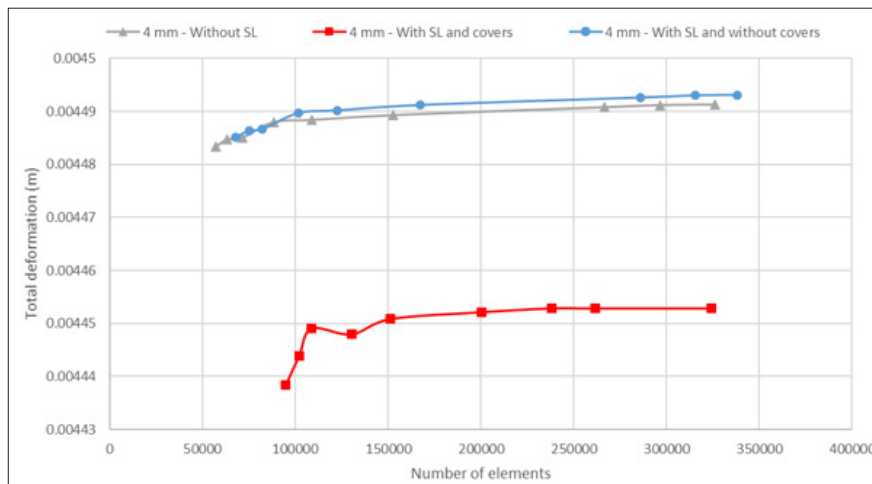


Figure 46: Total deformation for model 2

Regarding the maximum stress, it was increased for variant 2 (by around 6 times) and variant 3 (by around 1.2 times). For variant 2 the maximum stress was on the right cover of rib 5, while the other cases showed the maximum stress at the trailing edge of the first rib.

Table 7: Summary for model 2 – rib with 4 mm web thickness

	Variant 1	Variant 2	Variant 3
Maximum deformation (mm)	4.4912	4.4528	4.4930
Deformation difference (%)	-	-0.86	0.04
Location	Wing tip	Wing tip	Wing tip
Maximum stress (MPa)	45.25	282.68	55.84
Stress difference (%)	-	624.67	123.39
Location	Rib 1	Right cover rib 5	Rib 1

Model 3 was 3 mm rib thickness with 6 mm upper and lower caps. As in model 2, there was little difference of deformation between variants 1 and 3. Variant 2 presented similarities to wing rib model 1, since the total deformation curves oscillated, but the oscillation was less for model 2. In all cases, the location of the maximum deformation is on the wing surface close to the wing tip.

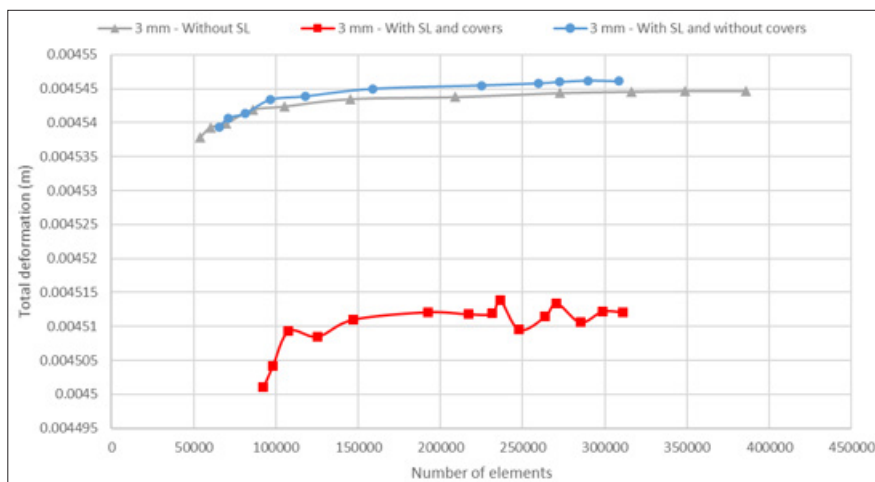


Figure 47: Total deformation for model 3

The maximum stress was increased for variant 2 (by around 200 %) and variant 3 (by around 90 %). The location of the maximum stress for variant 2 was found on the middle SL of the fourth rib, while in the other two cases was found on the trailing edge of the first rib.

Table 8: Summary for model 3 – rib with 3 mm web thickness

	Variant 1	Variant 2	Variant 3
Maximum deformation (mm)	4.5447	4.5121	4.5460
Deformation difference (%)	-	-0.70	0.03
Location	Wing tip	Wing tip	Wing tip
Maximum stress (MPa)	52.64	119.98	48.75
Stress difference (%)	-	205.35	92.60
Location	Rib 1	Middle SL rib 4	Rib 1

Figure 48 shows an overview of the total deformation curves for the three wing rib models and each variant. The maximum deformation values were found for model 3. Model 1 presented less deformation compared to the other two models. Model 2 presented no oscillations in variant 2, opposite to the other two models.

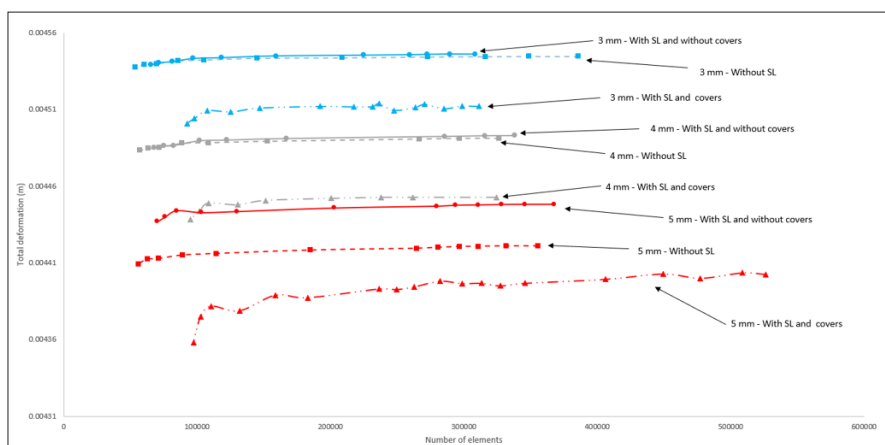


Figure 48: Overview of total deformation for the three wing rib models

Model 1 and model 3 showed similarities in their stress distribution. For model 2 less deformation was found for variant 1 and the stress for variant 3 was higher (by around 1.2 times). In the three models, the maximum stress was found for variant 2. From the simulation results, it can be stated that the three wing rib models are suitable for AM manufacturing. Their maximum stress under the considered loading conditions is lower than the tensile ultimate strength of the Al 7050-T7451 (524 MPa). In addition, their maximum deformation is around 0.26 % with respect to the half wingspan (1,710 mm), which is not significant. For the next stage of the DfAM (design process), model 3 is more suitable for embedding sensory capability for two reasons. Firstly, from the simulations point of view, it presented less stress than the other two models. Secondly, when considering factors influencing the selection between

AM and conventional processes, such as lightweight design and process cost comparison, model 3 allows a more lightweight part and less manufacturing time and costs.

Conclusions and Future Work

The scope of this paper was to propose a design of a wing rib with sensory capability which could be used within an Industry 4.0 ecosystem with structural features suitable for reproduction using additive manufacturing technique. The goal was to ascertain the structural integrity of the design for additive manufacturing. The wing rib design was done in Catia using NACA 0018. Cut-outs were performed to reduce weight and to increase load resistance. Besides, cut-outs are used to allow the wing interior equipment to pass through the ribs. Ansys was used to simulate three five-rib wing models with and without sensory locations. For the simulation models, boundary conditions for a single rib are not trivial, and current research does not provide a guideline to simulate a single rib. In this work, simulations were done considering the operating empty mass of the Boeing 747-400 and its wing surface. An equivalent force for the wing model was calculated and used as boundary condition. The second boundary condition consisted of maintaining the wing root fixed to the fuselage as real wings. The simulation results showed that the total deformation does not represent a significant variation between the cases “Without SL” and “With SL and without covers”, while the case “With SL and covers” showed less deformation. In all cases, the maximum deformation was on the wing surface close to the wing tip. The equivalent von-Mises stress is highly affected by embedding sensory capability considering the case with sensory covers.

Sensory integration allows collection of life cycle data in aircraft wing ribs that can be used for drifting away from the condition-based preventive maintenance system to a data-driven predictive maintenance-based system. The use of AM when embedding sensors allows more flexibility without compromising the structural integrity of parts. Besides, the implementation via AM processes has the advantage of design freedom and limited costs when modifying geometries.

Future works will tackle the additive manufacturability design aspect. The next stage will be to implement this design via additive manufacturing process before experimental trials at various scales. Based on the simulation results, the next step will be dealing with the re-designing of an AM manufacturing process for the rib geometry 3 mm web thickness with 6 mm upper and lower caps, considering embedded sensory capability.

Author Contributions

Conceptualization, R. Dogea; methodology, R. Dogea.; software, R. Dogea.; validation, R. Dogea; formal analysis, X. T. Yan, R. Millar and R. Dogea.; investigation, R. Dogea.; resources, R. Dogea.; data curation, R. Dogea.; writing—original draft preparation, R. Dogea.; writing—review and editing, X. T. Yan and R. Millar; visualization, X. T. Yan and R. Millar; supervision, X. T. Yan and R. Millar; project administration, R. Dogea.; funding acquisition, X. T. Yan and R. Millar. All authors have read and agreed to the published version of the manuscript.

Acknowledgments

The authors acknowledge the support of the National Manufacturing Institute Scotland and the Department of Design, Manufacturing and Engineering Management of the University of Strathclyde, United Kingdom.

Conflicts of Interest

The authors declare no conflict of interest.

References

1. Bristow JW, Irving PE (2007) Safety factors in civil aircraft design requirements. *Eng. Fail. Anal* 14: 459-470.
2. Daily J, Peterson J (2017) Predictive Maintenance: How Big Data Analysis Can Improve Maintenance In Supply Chain Integration Challenges in Commercial Aerospace; Springer International Publishing: Cham 267-278-p.
3. Liu C, Vengayil H, Lu Y, Xu X (2019) A Cyber-Physical Machine Tools Platform using OPC UA and MTConnect. *J Manuf Syst* 51: 61-74.
4. Rodrigue H, Rivette M (2010) An Assembly-Level Design for Additive Manufacturing Methodology. *IDMME*.
5. Hürlimann F, Kelm R, Dugas M, Kress G (2012) Investigation of local load introduction methods in aircraft pre-design. *Aerosp. Sci. Technol* 21: 31-40.
6. Kalavagunta V, Hussain S (2018) Wing Rib Stress Analysis of DLR-F6 aircraft. *IOP Conf. Ser. Mater. Sci. Eng* 455: 012033.
7. Dharmendra P, Chaithanya KJ, Sameera A, Kavathiya K, Monika KM (2020) Design and Analysis of an Aircraft Wing Rib for Different Configurations 7: 180-192.
8. Stolarski T, Nakasone Y, Yoshimoto S (2018) Fundamentals of the finite element method. In *Engineering Analysis with ANSYS Software*; Elsevier 1-35-p.
9. Thompson MK, Thompson JM (2017) Introduction to ANSYS and Finite Element Modeling. In *ANSYS Mechanical APDL for Finite Element Analysis*.
10. Yelluri Shwetha (2018) Buckling Analysis of Carbon Epoxy Trailing Edge Wing Rib. *Int. J. Mech. Prod. Eng. Res. Dev* 8: 659-670.
11. TU Delft Structures Aircraft & spacecraft wing structures 2011.
12. Bennaceur MA, Xu Y, Layachi H (2017) Wing Rib Stress Analysis and Design Optimization Using Constrained Natural Element Method. *IOP Conf. Ser. Mater. Sci. Eng* 234: 12018
13. Sharma R, Garg G (2014) Design and Analysis of Wing Rib of Aircraft Review. *Int. J. Innov. Res. Sci. Eng. Technol* 03: 12.
14. Choi Y, Abbas SH, Lee JR (2018) Aircraft integrated structural health monitoring using lasers, piezoelectricity, and fiber optics. *Meas. J. Int. Meas. Confed* 125: 294-302.
15. Gibson I, Rosen D, Stucker B, Khorasani M (2021) Development of Additive Manufacturing Technology. In *Additive Manufacturing Technologies*; Springer International Publishing: Cham 23-51-p.
16. Meisel N, Williams C (2015) An Investigation of Key Design for Additive Manufacturing Constraints in Multimaterial Three-Dimensional Printing. *J. Mech. Des* 137: 111406-111415.
17. Meng L, Zhang W, Quan D, Shi G, et al., (2020) From Topology Optimization Design to Additive Manufacturing: Today's Success and Tomorrow's Roadmap. *Arch. Comput. Methods Eng* 27: 805-830.
18. Hossain MS, Gonzalez JA, Hernandez RM, Shuvo MAI, et al., (2016) Fabrication of smart parts using powder bed fusion additive manufacturing technology. *Addit. Manuf* 10: 58-66.
19. Ansys, I. ANSYS Meshing Advanced Techniques; Ansys, Ed.; Canonsburg, PA, 2017.
20. Carneiro PMC, Gamboa P (2019) Structural analysis of wing ribs obtained by additive manufacturing. *Rapid Prototyp. J* 25: 708-720.
21. Kavya G, Cam MTCAD (2017) Design and Finite Element

- Analysis of Aircraft Wing Using Ribs and Spars. Int. Res. J. Eng. Technol.
22. Arunkumar KN, Lohith N, Ganesha BB (2012) Effect of Ribs and Stringer Spacings on the Weight of Aircraft Structure for Aluminum Material. J. Appl. Sci 12: 1006-1012.
 23. Vergün T, Tola C (2019) Rib Spacing Optimization of a Generic UAV Wing to Increase the Aeroelastic Endurance. In Proceedings of the 4th International Symposium on Innovative Approaches in Engineering and Natural Sciences Proceedings; SETSCI 108-111-p.
 24. Megson THG (2016) Aircraft structures for engineering students: Sixth edition; Butterworth-Heinemann.
 25. Niu MCY (1998) Airframe Structural Design: Practical Design Information and Data on Aircraft Structures.
 26. Blanco D, Rubio EM, Marín MM, Davim JP (2020) Repairing Hybrid Mg–Al–Mg Components Using Sustainable Cooling Systems. Materials (Basel) 13: 393.
 27. Stettenheim P (1997) The Simple Science of Flight: From Insects to Jumbo Jets Henk Tennekes. Condor 99. doi:10.2307/1370501.
 28. Rinku A, Ananthasuresh GK (2015) Topology and Size Optimization of Modular Ribs in Aircraft Wings. 11th World Congr. Struct. Multidiscip. Optim.
 29. Sinha K, Klimmek T, Schulze M (2021) Loads analysis and structural optimization of a high aspect ratio, composite wing aircraft. CEAS Aeronaut J 12: 233-243.
 30. Stoll P, Schmid M, Von Ohr MS, Wegener K (2020) Integration of acceleration sensors in polymer parts produced with selective laser sintering. In Proceedings of the AIP Conference Proceedings 2205: 020063.
 31. Juhasz M, Tiedemann R, Dumstorff G, Walker J, et al., (2020) Hybrid directed energy deposition for fabricating metal structures with embedded sensors. Addit. Manuf 35. doi:10.1016/j.addma.2020.101397.
 32. Cavdir D (2020) Embedding electronics in additive manufacturing for digital musical instrument design. In Proceedings of the Proceedings of the Sound and Music Computing Conferences.
 33. Hossain MS, Gonzalez JA, Hernandez RM, et al., (2017) Smart parts fabrication using powder bed fusion additive manufacturing technologies. In Proceedings of the Solid Freeform Fabrication 2017: Proceedings of the 28th Annual International Solid Freeform Fabrication Symposium - An Additive Manufacturing Conference, SFF.
 34. Rub J, Bahemia H (2019) A Review of the Literature on Smart Factory Implementation. In Proceedings of the 2019 IEEE International Conference on Engineering, Technology and Innovation (ICE/ITMC); IEEE 1-9-p.
 35. Niccolai L, Bassetto M, Quarta AA, Mengali G (2019) A review of Smart Dust architecture, dynamics, and mission applications. Prog. Aerosp. Sci 106: 1-14.
 36. Agogino AM, Tumer I (2006) Integrated Systems Health Monitoring Using Smart Dust Mote Sensor Networks.
 37. Marias GF, Barros J, Fiedler M, Lima L, Lorentzen C, et al. (2012) Security and privacy issues for the network of the future. Secur. Commun. Networks 5: 987-1005.

Copyright: ©2021 Ramona Dogea, et al. This is an open-access article distributed under the terms of the Creative Commons Attribution License, which permits unrestricted use, distribution, and reproduction in any medium, provided the original author and source are credited.